Materialia 9 (2020) 100535

Contents lists available at ScienceDirect

Materialia

journal homepage: www.elsevier.com/locate/mtla

Full Length Article

Revealing intrinsic lattice expansion and grain boundary excess volume of nanocrystalline Se prepared via various methods

Lei Gu, Yonghao Zhao*

Nano and Heterogeneous Materials Center, School of Materials Science and Engineering, Nanjing University of Science and Technology, Nanjing 210094, China

ARTICLE INFO

Keywords:
Lattice expansion
Grain boundary excess volume
Nanocrystalline materials

ABSTRACT

Nanocrystalline (nc) materials possess a large fraction of grain boundaries (GBs) with excess free volume which is expected to exert a tensile stress field to nano-crystallites and cause a lattice expansion (Gleiter, 1989). However, experimental investigations on the lattice constants of nc materials show ambiguous results indicating either lattice contraction or expansion. To clarify the contradictory results, in this work nc Se specimens with different grain sizes were prepared by mechanical milling of crystalline Se and nanocrystallization of amorphous Se solid under high pressure (1 GPa). Quantitative x-ray diffraction measurements revealed that the nc Se specimens exhibit significantly large intrinsic lattice expansions with decreasing grain size, which are also noted to depend on synthesis route. The measured unit cell volumes of nc Se were well fitted using a GB stress field model from which the calculated GB excess free volume also shows processing method dependence. Our results suggest an intrinsic lattice expansion in nc Se.

1. Introduction

Lattice constant/parameter is one of the most principle structure quantities of a crystal because it critically governs physical (e.g., electronic, magnetic, optical, thermal, etc.,), chemical (e.g., catalytic, cohesive, etc.), mechanical (e.g., modulus of elasticity, etc.) and thermodynamic (e.g., phase instability, stacking fault energy, etc.) properties [1–15]. For examples, lattice expansions of α-Fe and VO_2 thin films with thicknesses in nanometer scale were reported to elevate magnetic moments and to suppress metal-to-insulator transition, respectively [1,2]. First-principle calculations based on density functional theory indicate that stacking fault energy in f.c.c. Fe increases with thermal lattice expansion [3]. In addition, experiments also reveals that lattice expansions of Si [4,5], Ge [6], Se [7–9] and CeO_2 [10] can induce crystal-to-amorphous phase transformation. Physical modeling using a hard-sphere approach shows the lattice expansion leads to an increase in cohesive energies, a bond weakening and a suppression in Young's modulus of nc materials [11,12]. Conversely, by tailoring the lattice constant materials scientists can control or alter the above properties to satisfy industrial application requirements. The equilibrium lattice constant is controlled by a local balance between short-range repulsive and long-range Coulomb forces. In practice, the lattice constant can be modified by controlling the following several factors as surface/boundary/interface, lattice solute/defect and external conditions (e.g. temperature, stress, excitation, impact ionization, etc.) [13–18].

Nanocrystalline (nc) materials possess a small grain size usually less than 100 nm [19,20], implying an increased grain boundary (GB) volume fraction which is almost 50% at a grain size of 2.5 nm. Accordingly, nc materials are considered to be inherently heterogeneous, composed of nano-crystallites embedded in a GB network [21]. Experimental studies of positron annihilation and transmission electron microscopy on nc materials revealed the presence of single vacancy in excess and vacancy clusters/voids [22–24] as well as a highly disordered structure [25] at GBs, which give rise to the notion of GB excess free volume ΔV_{nc}^{GB} [26–28]. A larger ΔV_{nc}^{GB} corresponds to a more disordered GB structure and a higher GB enthalpy. The ΔV_{nc}^{GB} is expected to generate tensile stress fields to the surrounding lattices of nano-crystallites and thus induces lattice expansions of nc materials [29,30]. However, experiments revealed an ambiguous result on the lattice parameter change of nc materials, i.e., both lattice expansion and contraction are reported, as summarized in Table 1.

It is obvious that evident lattice expansions (0.2–0.3%) occurred in nc Si [4,5], Ge [6] prepared by mechanical milling (MM), and Se [14,31] metalloids by nanocrystallization of amorphous solids (NAS), of which variations are one order of magnitude larger than those in pure metals (several of ten thousandth). For metals, lattice expansion was reported in nc Cr prepared by inert gas condensation following by subsequent consolidation (IGC) [32] and Fe by MM [33], while lattice contraction was observed in nc W by MM [33] and Cu by severe plastic deformation (SPD) [34]. Moreover, both lattice expansion and contraction are

* Corresponding author.
E-mail address: yhzhao@njust.edu.cn (Y. Zhao).

https://doi.org/10.1016/j.mtla.2019.100535
Received 13 October 2019; Accepted 21 November 2019
Available online 22 November 2019

Table 1
A list of the lattice parameter changes ($\Delta a = =(a–a_0)/a_0$, $\Delta c = =(c–c_0)/c_0$, where a_0 and c_0 are the equilibrium tabulated values) and the calculated GB excess volume ΔV_{nc}^{GB} based on Eq. (5) in various nc samples processed by means of different techniques (IGC = inert gas condensation following by subsequent consolidation, MM = =mechanical milling, SPD = =severe plastic deformation, NAS = nanocrystallization of amorphous solids).

Sample	D (nm)	Synthesis	Lattice change (%)	ΔV_{nc}^{GB} (%)	Reference
Cr	11	IGC	$\Delta a = =+0.04$	1.44	[32]
W	30	MM	$\Delta a = =-0.016$	−2.30	[33]
Fe	10	MM	$\Delta a = =+0.02$	0.98	[33]
Ni	14	MM	$\Delta a = =+0.01$	0.67	[33]
	25	MM	$\Delta a = =-0.01$	−1.19	[33]
Cu	85	SPD	$\Delta a = =-0.001$	−0.40	[34]
	11	MM	$\Delta a = =0$	0.0	[35]
	20	MM	$\Delta a = =+0.007$	0.66	[33]
	33	MM	$\Delta a = =-0.004$	−1.08	[33]
Pd	>8	IGC	$\Delta a = =-0.03$	−1.12	[36]
	<8	IGC	$\Delta a = =+0.02$	0.75	[37]
Si	8	MM	$\Delta a = =+0.20$	7.2	[4,5]
Ge	4	MM	$\Delta a = =+0.20$	3.6	[6]
Se	13	NAS	$\Delta a = =+0.30$	–	[14,31]
			$\Delta c = =-0.12$		

simultaneously observed in the same systems of nc Ni, Cu [33,35] and Pd [36,37] or in the same experiments of MM [33,35] and IGC [36,37]. For instance, nc Pd exhibits a lattice expansion when grain size is smaller than 8 nm [36] and a lattice contraction when grain size is larger than 8 nm [37]. More recently, a non-monotonic variation of the lattice parameter with grain size was reported in nc Ni and Cu prepared by MM, exhibiting a transformation from lattice contraction to lattice expansion with decreasing grain size [33]. These complicated or even contradictory results of the lattice parameter changes in nc materials might be stemmed from several extraneous factors, such as residual stresses induced by non-equilibrium IGC, NAS and SPD processing and impurities (such as O and N etc.) introduced by MM. Moreover, measurement errors, associated with peak broadening and weakening, peak shifting, and non-symmetries because of the interactions of x-rays and/or neutrons with nanometer-sized crystallites [38], may affect the experimental determination of lattice parameter. Hence, partially due to conflicting results from published studies, and partially because of these experimental challenges, it remains mostly unanswered about the question whether nc materials exhibit inherent variations in lattice parameter.

In the present study, motivated by the above question we chose trigonal Se as a model material and systematically studied its lattice parameter variations with grain size. We employed MM and NAS under high pressure (MASHP) to synthesize nc Se specimens with varying grain sizes. As shown in Fig. 1 [39], elemental Se has special structure of helical $[–Se–]_n$ molecular chains with intra-chain covalent bonds and inter-chain Van der Waals forces. Lattice parameter a is the distance between the $[–Se–]_n$ chains which is bonded by weak van der Waals force. The van der Waals force is about one order of magnitude smaller than those of metallic and covalent bonds. Therefore, a value could be easily expanded if the GB stress works on these $[–Se–]_n$ chains in grain interiors.

2. Experimental procedures

2.1. Sample preparations

For the mechanical milling process, a high-energy vibratory ball mill with stainless steel balls and vial was employed to mill pure Se powders (with a purity of 99.999% and particle size smaller than 600 mesh) at ambient temperature. The ball-to-powder weight ratio was selected as 10:1. To avoid oxidation, about 4.5 g Se powder was first charged into the vial and sealed by an elastic O-ring, then the vial was evacuated with a vacuum of 3×10^{-3} Pa and then filled under dry Ar atmosphere (O_2, H_2

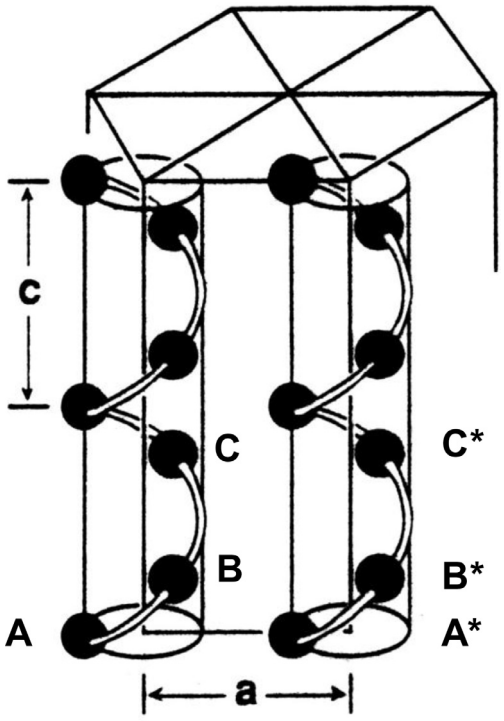

Fig. 1. Schematic representation of the helical trigonal Se structure [39].

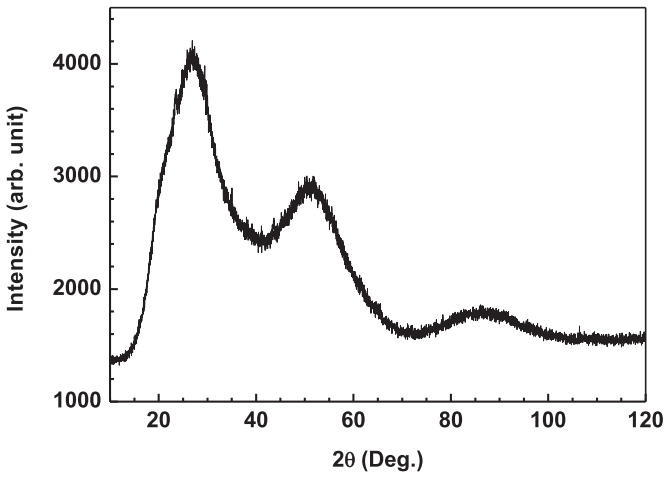

Fig. 2. X-ray diffraction patterns of the relaxed as-quenched amorphous Se. Three broad scattering peaks are characteristic of amorphous Se.

<5 ppm) with an over-pressure of about 3×10^5 Pa. For each mechanical milling procedure, a new batch of initial powder was used and milled without interruption. In the milled sample, the O and N contents were less than 0.1 wt% and the Fe content less than 0.02 wt%, as analzed by wet chemical analysis and energy-dispersive x-ray analysis.

For NAS under high pressure, the molten Se was first sealed in a quartz ampoule evacuated to 1.33×10^{-2} Pa and melted at 673 K for 60 min, then was quenched into the liquid nitrogen to produce an amorphous Se (a-Se) solid. The as-quenched a-Se, still sealed in vacuum quartz, was maintained at 333 K for 400 h to attain full structure relaxation. Fig. 2 displays X-ray diffraction patterns of the relaxed as-quenched amorphous Se. Three broad scattering peaks are characteristic of amorphous Se. The relaxed a-Se pieces (about 4–5 g) were then grounded by using fine grinding papers for NAS at high pressure. A piston-cylinder pressure vessel with an internal diameter of 8 mm was

used at a pressure of 1.0 GPa in a vacuum furnace. The accuracy of the applied pressure is about ±1%. To monitor the sample temperature, a thermocouple was placed under the vessel. The difference between the temperature measured by the thermocouple and the actual temperature of the specimen in the vessel was less than 3 K, and all the resultant temperatures have been amended. The amorphous Se specimen was placed into the cylinder vessel with fine NaCl powder as a pressure medium and a vacuum of 3×10^{-3} Pa. Before heating, the specimen in a NaCl capsule was compressed at a pressure of 1.1 MPa for 30 min to minimize the pressure reduction induced by structure relaxation during the experiment. After the pressure was reduced to 1 GPa, the pressing piston was fixed and the specimen was heated at a heating rate of 10 K/min to a given annealing temperature (from 450 to 570 K) for 1.5 h for complete nanocrystallization. The relative error for the heating rate is about 25%.

2.2. Microstructural characterizations

Rigaku D/MAX 2400 x-ray diffractometer with a wide angle goniometer was employed to perform the quantitative x-ray diffraction (XRD) measurements of the different grain-sized nc-Se samples. For XRD measurements, the milled and crystallized nc-Se powders were filled in the groove of the XRD specimen holder. To increase the diffraction peak intensity, a rotating Cu target with a voltage of 50 kV and a current of 100 mA was used. A graphite crystal <0002> scattering at the goniometer receiving slit section was used to select the x-ray wavelengths λ_{ka1}(=1.54056 Å) and λ_{ka2} (=1.54439 Å). With these wavelengths, the extinction depth in Se was calculated to be less than 87 μm, which was much smaller than the thickness of the measured sample. Ensuring that the entire beam is either absorbed or diffracted by the sample, the divergence slit was selected with a width of 0.5° and placed in the incident x-ray beam. The scattering slit was also chosen with a width of 0.5° to control the scattering x-ray on the counter. The width of receiving slit was selected as 0.15 mm to controls the width of diffracted x-ray to be entered into the counter. The reflection mode with the scattering vector aligned approximately perpendicular to the sample surface was used for measurements of $\theta-2\theta$ scans for the samples. A small angular step of 2θ (0.02°) and a fixed counting time of 10 s were taken to measure the intensity of the Bragg reflections. For the rest of the XRD pattern, which is related to the background intensity, a step size of 0.1° and a counting time of 5 s were used. The scan range for 2θ was 20°–103° and the experimental temperature was 293 K.

Thermal analysis was performed using a Perkin–Elmer differential scanning calorimeter (DSC-7), with a sensitivity of 0.04 mJ/s for energy measurements. As-milled Se powder compact (of which the weight ranges from 10–25 mg) and nanocrystallized nc Se by NASHP as well as-quenched amorphous Se were sealed in Al pans and measured in a flowing Ar atmosphere at a constant heating rate of 10 K/min. The temperature was calibrated with pure In and Zn standard samples, with an accuracy of ±0.2 K.

Transmission electron microscopy (TEM) observations were conducted on a Philips EM 420 microscope operated at an accelerating voltage of 100 kV. The milled Se powders were first separated by ultrasonic vibration in an alcohol solution, then were collected and supported by Cu grids for TEM observations. The nanocrystallized nc Se sample was first sealed in a Cu tube with a diameter of 3 mm, and then was cut, together with Cu tube, into thin disks with a thickness of 0.5 mm and a diameter of 3 mm. The Se thin piece, supported by Cu ring, was mechanically ground and dimpled with diamond slurries as well as ion-milled by Ar+ ion to obtain an electron transparency foil. The morphology of the milled Se powder was imaged by a FEI-XL30 SFEG scanning electron microscopy (SEM) using a 25 kV beam.

3. Data evaluation

To calculate grain size, microstrain and lattice parameters, the XRD Bragg diffraction lines are fitted by using the Pseudo-Voigt function (a linear combination of Lorentzian and Gaussian functions [38,40]) from which the Lorentzian and Gaussian fractions, integral width and peak position could be obtained.

On the basis of an XRD peak broadening method, the grain size of the nc Se samples was calculated. The peak broadening is characterized by its integral width. The measured intensity profile of the Bragg reflection is a convolution of a instrumental broadening profile with the physical intensity profile. The instrumental broadening profile determined by means of a SiO_2 reference sample is revealed as to be a Gaussian type [14].The measured profile of the Bragg reflection in the nc-Se sample possesses primarily a Lorentzian component [14]. By supposing that the physical profile of the nc Se is primarily a Lorentzian type, the physical intensity profile can be separated from the measured intensity profile by removing the instrumental broadening effect. Small crystallites and the presence of microstrain within the specimen can result in the microstructure broadening of the sample. Therefore, the physical broadening profile can be considered as the convolution of the grain-size broadening

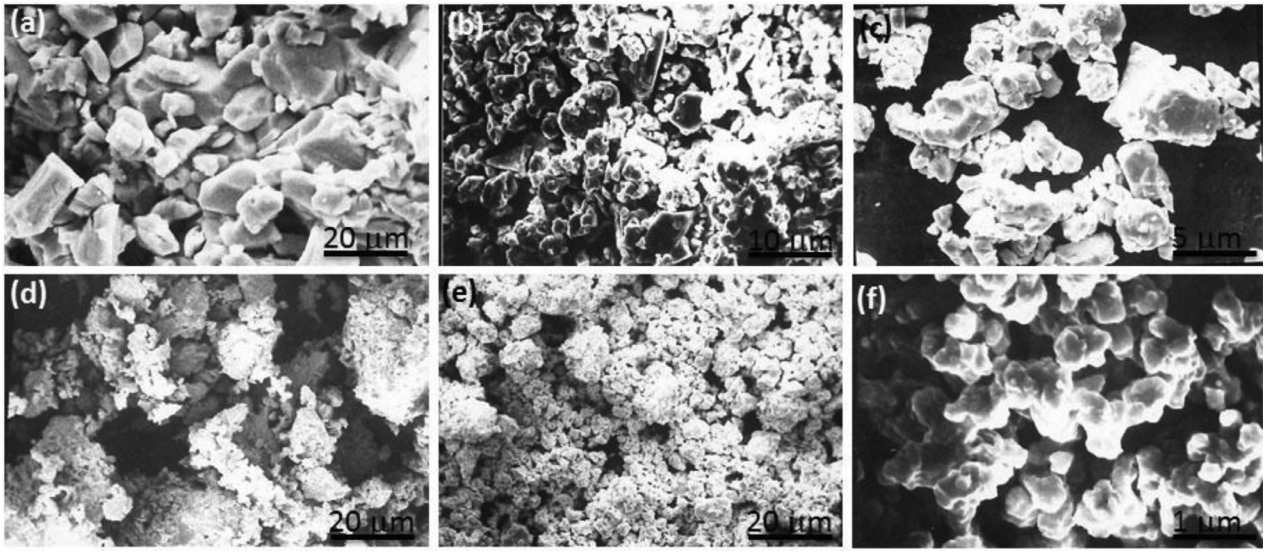

Fig. 3. SEM images of the milled Se samples with 0 min (a), 5 min (b and c), 20 min (d) and 30 min (e,f).

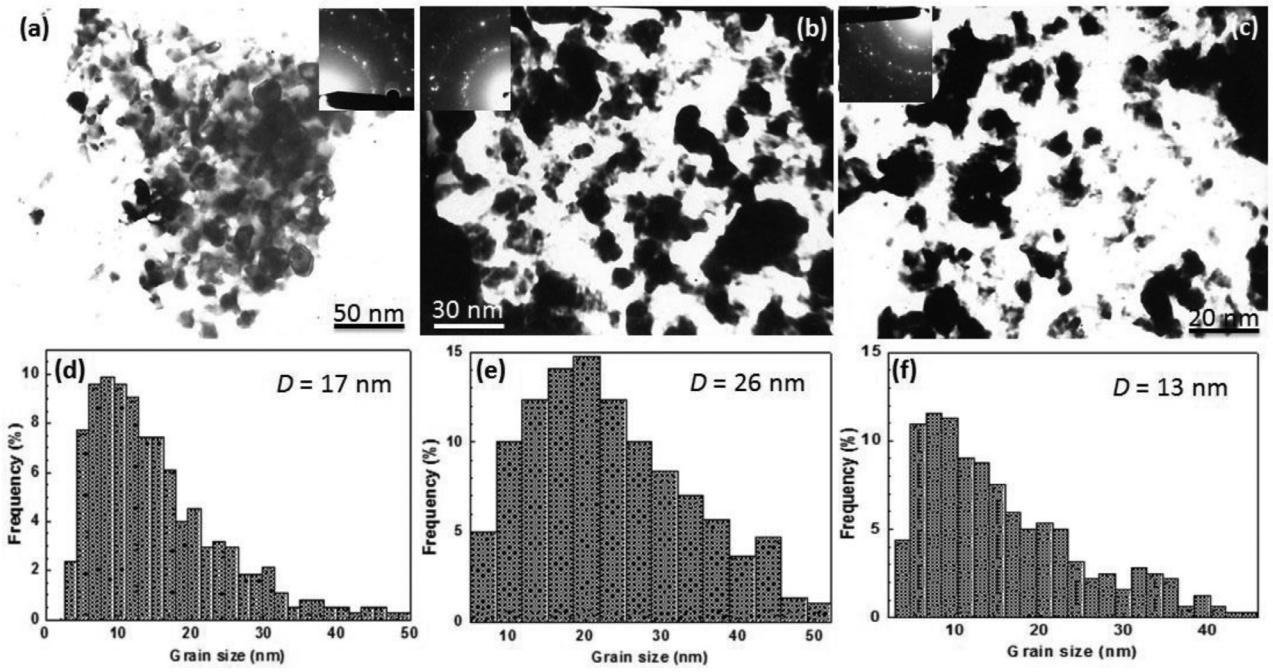

Fig. 4. TEM images of the milled nc Se sample with 30 min (a) and nanocrystallized nc Se samples with 490 K (b) and 450 K (c) as well as their corresponding selected area electron diffraction (SAED) patterns (insets) and grain size distributions (d–f).

profile (usually represented by a Lorentzian function [38]) with that of the microstrain broadening (a Gaussian function [41]). Then the grain size and the microstrain of the sample can be calculated from the integral width of the physical broadening profile in terms of the Scherrer and Wilson equation [41]:

$$\frac{\beta_{hkl}^2}{tg^2\theta_{hkl}} = \frac{\lambda\beta_{hkl}}{D_{hkl}tg\theta_{hkl}\sin\theta_{hkl}} + 16\left\langle\varepsilon_{hkl}^2\right\rangle^{1/2}, \quad (1)$$

where λ is the wavelength of Cu $K_{\alpha 1}$ irradiation, D_{hkl} and $\langle\varepsilon_{hkl}^2\rangle^{1/2}$ represent the thickness and the mean magnitude of microstrain of the grains in the $\langle hkl\rangle$ direction, respectively. By performing a least-square fit to $\beta_{hkl}^2 / tg^2\theta_{hkl}$ plotted against $\lambda\beta_{hkl} / (tg\theta_{hkl}sin\theta_{hkl})$ for all of the measured peaks of the samples, the mean grain size D and the mean microstrain $\langle\varepsilon^2\rangle^{1/2}$ can be determined. Standard linear regression techniques provide an estimate for the uncertainty in the parameters from the error in the fit [42].

Determination of the lattice parameters in nc Se includes two stages. First, the modified Rachinger method was used to remove the λ_{ka2} component from the XRD profiles [43,44] Second, the intensity peak centroid positions was used to calcualte the lattice parameters for the nc-Se specimens. The external standard method using a pure Si polycrystal was employed to calibrate the peak positions in order to minimize the system error. The calibration function was:

$$\Delta 2\theta = \alpha + \beta\cos\theta + \gamma\sin\theta, \quad (2)$$

where α relates to 2θ-axis origin displacement, β relates to eccentricity between the sample and goniometer center axis, and γ relates to the sample flatness or absorption. In this study, α, β and γ were determined by the least-square method, being 0.013891, −0.080571, and 0.023696, respectively. Considering that the nc Se is the trigonal structure, the weighted least-square method was selected to calculate the lattice parameters in order to minimize the calculation error. The equation is originated from the Bragg's law and given by

$$\frac{h^2a*}{2} + \frac{k^2b*}{2} + \frac{l^2c*}{2} + \frac{2klb*c*}{\cos\alpha*} + \frac{2lha*c*}{\cos\beta*} + \frac{2hka*b*}{\cos\gamma*} + E(\theta)x = \frac{4\sin^2\theta}{\lambda^2} \quad (3)$$

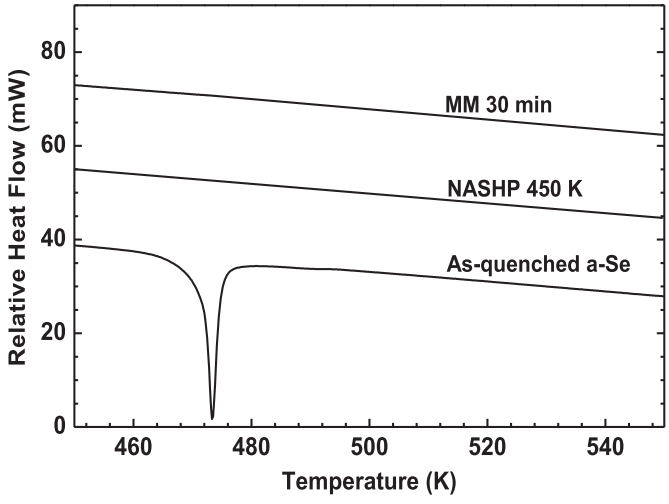

Fig. 5. DSC curves of the as-quenched amorphous Se, milled nc Se with 30 min and nanocrystallized nc Se with 450 K. The exothermic peak at 473 K is corresponding to crystallization of amorphous Se.

where a^*, b^*, c^* and α^*, β^*, γ^* are the reciprocal-lattice parameters from which the lattice parameters of the nc Se can be obtained. $E(\theta)$ is the error function that is selected as $\sin^2 2\theta$ and x is the error function weight. The values of the lattice parameters of the nc Se were finally calculated from the intensity centroid positions of nine single peaks (100), (101), (200), (201), (210), (211), (113), (104) and (302).

4. Results

The as milled Se powder has a particle size in micrometer range, as shown in Fig. 3(a), and was refined and spheroidized significantly when milling time is 5 min (Fig. 3(b) and (c)). When milling time is 20 min, micrometer-sized agglomerates with finer particle size below 1 μm were formed, as shown in Fig. 3(d). Further milling up to 30 min resulted in a

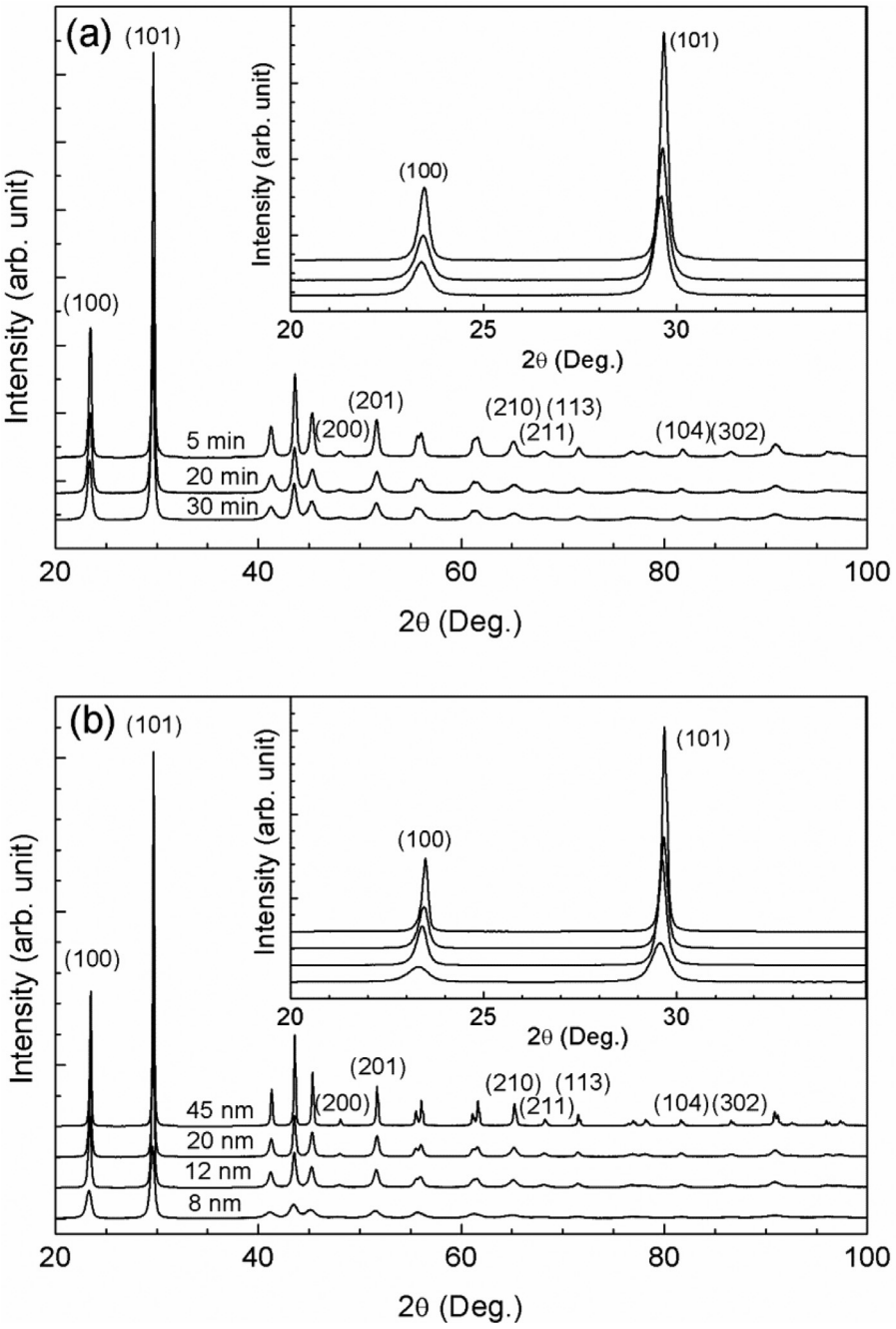

Fig. 6. X-ray diffraction patterns of (a) the milled and (b) nanocrystallized nc Se samples with different milling time and annealing temperatures, as marked in the figures.

more uniform and finer agglomerates, as shown in Fig. 3(e) and (f). TEM image revealed that the fine particles with a size below 1 μm, formed agglomerates in SEM images, were further composed of nanocrystalline grains with an average grain size of about 17±5 nm (Fig. 4(a) and (d)). The selected area electron diffraction (SAED) pattern (inset in Fig. 4(a)) shows a continuous ring caused by a random grain orientation distribution. The TEM observations also discovered the Se samples prepared by NASHP have nanocrystalline grains, as shown in Fig. 4(b) and (c). The average grain sizes of the nc Se samples by NASHP with 490 K (Fig. 4(b)) and 450 K (Fig. 4(c)) are 26 ± 5 nm (Fig. 4(e)) and 13 ± 5 nm (Fig. 4(f)), respectively. The continuous SAED patterns in the insets revealed random grain microstructures with texture-free. Fig. 5 demonstrates DSC curves of the as-quenched amorphous Se, milled nc Se with 30 min and nanocrystallized nc Se with 450 K. The exothermic peak at 473 K is corresponding to recrystallization of amorphous Se. The DSC curves free of recrystallized exothermic peak of the milled nc Se with 30 min and nanocrystallized nc Se with 450 K indicate a complete recrystallization process during NASHP and a grain refinement process without amorphization during MM.

Fig. 6 shows typical XRD patterns for milled and nanocrystallized nc Se samples. The nc Se samples have a trigonal structure. It is obvious that with increasing milling time and decreasing annealing temperature, the Bragg diffraction lines are significantly broadened, and the peak positions shift towards lower 2θ values, suggesting a lattice expansion. However, the broad scattering peaks of amorphous Se, as shown in Fig. 2, were not observed, which further confirmed the above DSC results.

The calculated grain size and microstrain of the milled and nanocrystallized nc Se samples versus mechanical milling time and annealing temperature are shown in Fig. 7(a) and (b) and listed in Tables 2 and 3.

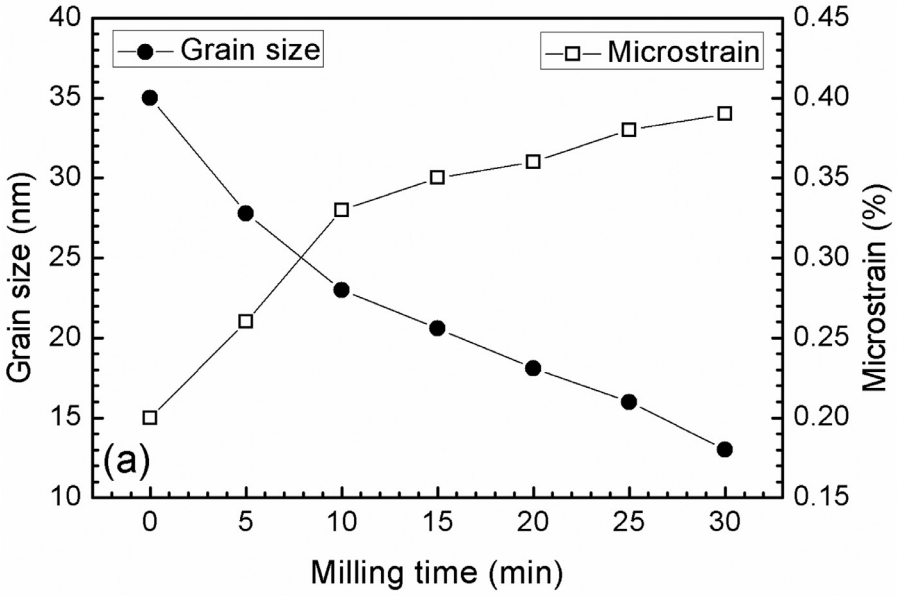

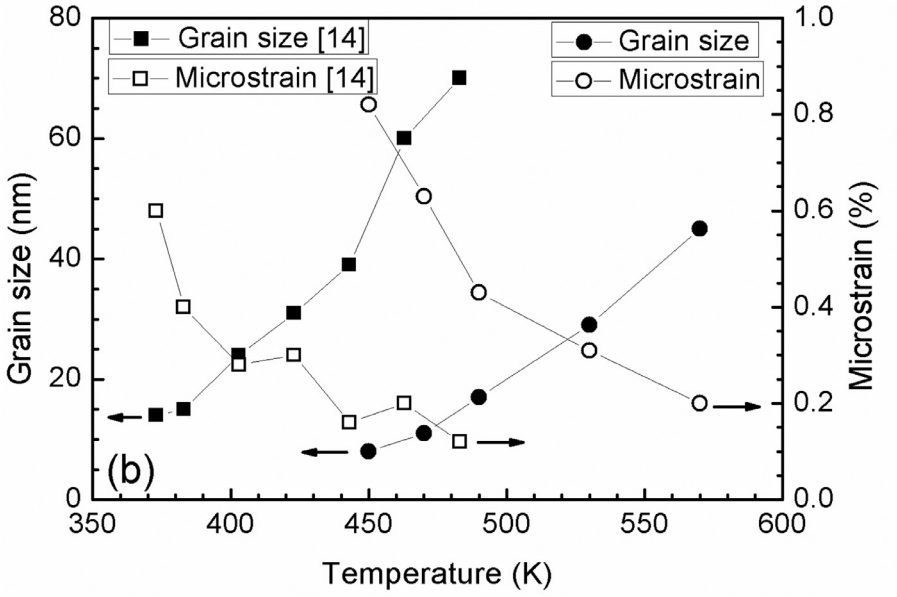

Fig. 7. (a) Milling time and (b) annealing temperature dependences of grain size and microstrain of nc Se (MM = mechanical milling, NASHP = =nanocrystallization of amorphous Se at high pressure). The grain size and microstrain measurement errors are ±2 nm and ±0.02%.

Table 2
A list of grain size *D*, microstrain$<\varepsilon^2>^{1/2}$, lattice parameters *a, c* and unit cell volume V_{nc}^{uc} of the nc Se by MM. The *D*, $<\varepsilon^2>^{1/2}$, *a, c* measurement errors are ±2 nm, ±0.02%, ±0.001 Å and ±0.001 Å.

Milling time (min)	*D* (nm)	$<\varepsilon^2>^{1/2}$ (%)	*a* (Å)	*c* (Å)	V_{nc}^{uc} (Å^3)
0	35	0.20	4.3660	4.9580	81.847
5	28	0.26	4.3666	4.9573	81.858
10	23	0.33	4.3664	4.9574	81.852
15	21	0.35	4.3666	4.9567	81.848
20	18	0.36	4.3669	4.9560	81.848
25	17	0.38	4.3679	4.9561	81.867
30	13	0.39	4.3702	4.9564	81.964

Table 3
A list of grain size *D*, microstrain$<\varepsilon^2>^{1/2}$, lattice parameters *a, c* and unit cell volume V_{nc}^{uc} of the nc Se by NASHP. The *D*, $<\varepsilon^2>^{1/2}$, *a, c* measurement errors are ±2 nm, ±0.02%, ±0.001 Å and ±0.001 Å.

Annealing temperature (K)	*D* (nm)	$<\varepsilon^2>^{1/2}$ (%)	*a* (Å)	*c* (Å)	V_{nc}^{uc} (Å^3)
450	8	0.82	4.3771	4.9575	82.256
470	11	0.63	4.3732	4.9579	82.116
490	17	0.43	4.3682	4.9580	81.931
530	29	0.31	4.3672	4.9594	81.915
570	45	0.2	4.3660	4.9595	81.872

Compared with the TEM results, XRD calculated grain size is slightly small. This is because XRD calculates the subgrain/domain size which is more sensitive than TEM observation. From Fig. 7(a), with increasing milling time, the grain size decreased gradually from 35 to 13 nm, and the microstrain increased from 0.20% to 0.39%. From Fig. 7(b), with decreasing annealing temperature, the grain size is reduced from 45 nm to 8 nm, and the microstrain increases from 0.20% to 0.82%. For comparison, the annealing temperature dependence of grain size

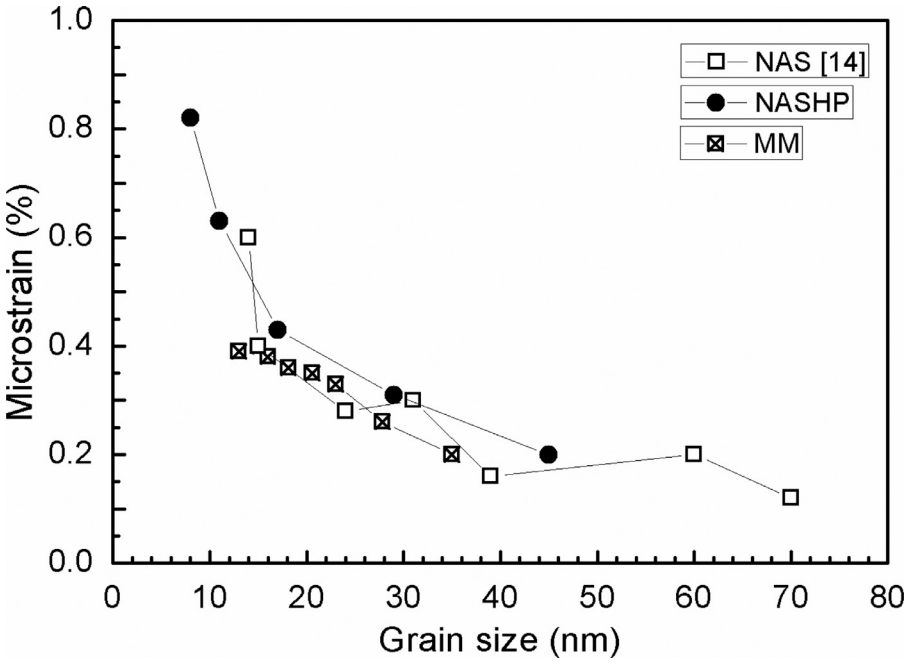

Fig. 8. Grain size dependence of microstrain of nc Se by NAS [14], MM and NASHP methods.

and microstrain of nc Se prepared by NAS at ambient pressure [14] was also shown in Fig. 7(b). One can see high pressure impeded nanocrystallization of a-Se by retarding crystallized temperature to higher values, resulting in a relative small grain size (8 nm) and high microstrain (0.81%). In Ref. 45, the pressure-induced enhancement in thermal stability of the amorphous Se against crystallization was analyzed in terms of the pressure effect on crystal nucleation kinetics, in which formation of the crystalline/amorphous interfaces is taken into consideration. Due to the excess volume of the crystal/amorphous interface, an overall volume expansion is involved in the crystal nucleation process when the nucleus size is very small. This effect leads to a significant increase in the critical work of nucleation when pressure is applied. Fig. 8 compares the grain size dependence of the microstrain in nc Se prepared by NAS [14], MM and NASHP, respectively. The microstrains of nc Se by different methods have similar variation versus the grain size, that is, increase with decreasing grain size. Moreover, the microstrain depends on systhesis route. For example, the microstrain of the milled nc Se is smaller than that of the nanocrystallized nc Se by NASHP under the same grain size.

The measured a and c for the nc Se samples with varying grain size were shown in Fig. 9(a) and (b) and listed in Tables 2 and 3. For comparison, the a and c values of the nc Se by NAS [14] were also drawn in the figures. The a of the nc Se samples prepared by NAS [14], NASHP and MM exhibit the similar variations against the grain size, i.e., increase with decreasing grain size. But the aD curve of the milled nc Se is lower than that of the nc Se by NASHP, which is further lower than that of the nc Se by NAS [14]. The largest a (D = 13 nm, by NAS) is about 0.29% larger than the equilibrium value a_0 (=4.3662 Å). The a change against grain size is far beyond the error bar which was estimated to be about 0.001 Å. The c values of the nc Se slightly decreases with decreasing grain size. Specifically, the c values of the milled nc Se are smaller than those of the equilibrium value c_0 (=4.9580 Å), while c values of the crystallized nc Se under ambient pressure are larger than that of the c_0, and the c values of the nc Se by NASHP are intermediate. With the measured a and c, the unit cell volume V_{nc}^{uc} of the nc Se samples can be calculated according to $V_{nc}^{uc} = \frac{\sqrt{3}}{2}a^2c$, as shown in Fig. 10. The values of V_{nc}^{uc} are found to be larger than the equilibrium data (V_0^{uc} = 81.8549 Å^3) for most of the nc Se specimens with small grain sizes, and increase with decreasing grain size, depending on the synthesis methodology used. The V_{nc}^{uc}-D curve of the nc Se by NAS [14] is higher than that of the nc Se by NASHP, which is further higher than that of the nc Se by MM.

5. Discussion

5.1. Microstrain and lattice expansion

As shown in Figs. 8–10, both microstrain and lattice expansion of the milled and nanocrystallized nc Se increase with decreasing grain size, and depend on synthesis routes. Specifically, the lattice expansion curve of the nc Se by NAS [14] is higher than that of the nc Se by NASHP, which is further higher than that of the nc Se by MM, and the microstrain versus grain size curve of the nc Se by NASHP is higher than that of the nc Se by MM. Therefore, the question of what is the relationship between microstrain and lattice expansion can be proposed naturally. As schematically shown in Fig. 11, microstrain represents the lattice distortion of grains. Due to the existence of microstress among grains, some grains were tensile, which are corresponding to a peak at lower 2θ angles in the XRD profile, and some grains were compressive corresponding to a peak at higher 2θ angles. Finally, the continuous peak moving towards both lower and higher 2θ angle results in the overall XRD peak broadening, from which the microstrain could be calculated. The lattice parameter represents the average lattice plane distance, and can be calculated from the overall XRD peak position. From Fig. 11, the overall peak position is same as the position of the peak corresponding to grains free of lattice distortion. When the overall peak moves towards lower 2θ angle, lattice expansion occurred, and vise versa. The increased lattice expansion with decreasing grain size was caused by the increase of GB volume fraction, as analyzed below. The increased microstrain with decreasing grain size was caused by the increased microstress among grains with increasing milling time or decreasing nanocrystallized temperature.

5.2. GB excess volume ΔV_{nc}^{GB}

The evident lattice expansions in the nc Se samples prepared by different methods appeared to be an intrinsic nature of nc Se materials, although the expansion amplitudes of the lattice parameters are dependent on the synthesis method used. To understand the lattice expansion phenomena, several models/approaches were proposed in

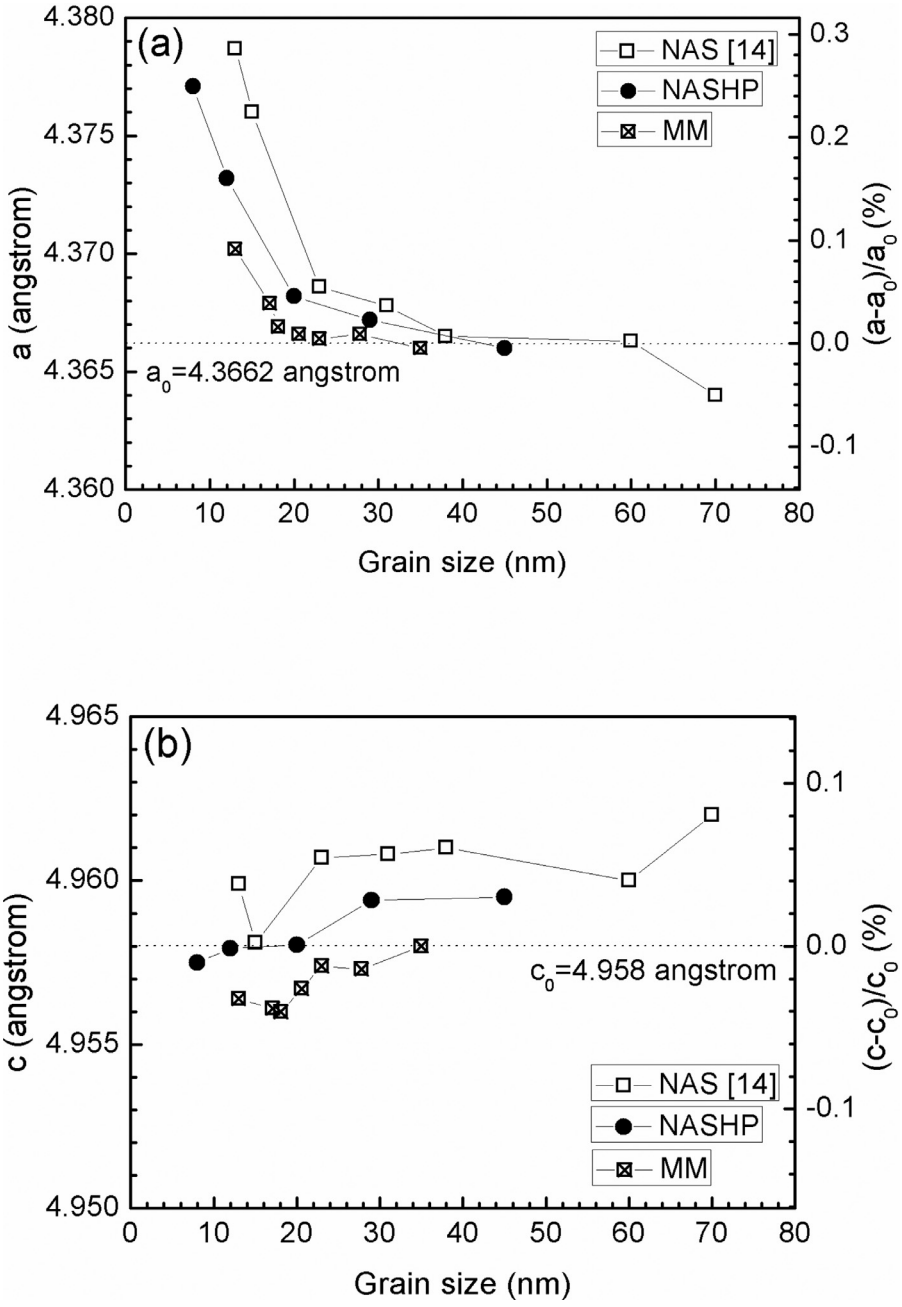

Fig. 9. Grain size dependence of the measured lattice parameters a (a) and c (b) as well as their deviations from the corresponding equilibrium values a_0 and c_0 of the nc Se samples prepared by different synthesis methods (NAS = nanocrystallization of amorphous Se [14]; MM = mechanical milling, NASHP = nanocrystallization of amorphous Se at high pressure). The error for a and c is about ±0.001 Å.

literature involving the effect of intra-crystalline pressure [46], interface stress [36,47,48], GB excess volume [49–52] and supersaturation of vacancies [53].

A model for the stress field generated by GB excess volume ΔV_{nc}^{GB} was developed by Qin et al. [50–52]. Because the density of the GBs is less than that of perfect crystallites, the ΔV_{nc}^{GB} is defined as

$$\Delta V_{nc}^{GB} = \frac{V_{nc}^{GB} - V_0^{pc}}{V_0^{pc}} \tag{4}$$

where V_{nc}^{GB} and V_0^{pc} are the molar volumes of the GBs and the perfect crystallites, respectively. $\Delta V_{nc}^{GB}$is one of the most appropriate quantities for elemental granular systems to describe the mechanical and thermodynamical properties of the GBs [28,54]. The GBs with excess free volume are non-equilibrium, of which atoms tend to shrink into perfect crystallites. Therefore the excess free volume at GBs due to vacancies in excess and vacancy clusters/voids [22–25,55,56] will induce a tensile stress field into nano-crystallites which diminishes according to $1/x^3$ [57,58], where x is the distance to the center of the defects at GBs. Under the tensile GB stress field, the atoms in nano-crystallites will deviate from their equilibrium sites, resulting in lattice expansion. According to the theory of elasticity [58] the displacement of an atom from its normal site will obey $1/x^2$. Assuming nc polycrystals consist of square-shaped nano-crystallites with orthogonal GB systems, the mean value of the total relative displacements of two adjacent atoms in the entire grain $\overline{\Delta r}$ can be given by

$$\overline{\Delta r} = \frac{r_0}{2D}\frac{\xi(\xi+2r_0)}{\xi+r_0}\left(\sqrt[3]{1+\Delta V_{nc}^{GB}}-1\right) \tag{5}$$

where ξ is the mean width of the GBs, D is the mean grain size, r and r_0 are the nearest-neighbor distance of a distorted and a perfect lattice. The unit cell volume expansion ΔV_{nc}^{uc} can be expressed as

$$\Delta V_{nc}^{uc} = \frac{3}{2D}\frac{\xi(\xi+2r_0)}{\xi+r_0}\left(\sqrt[3]{1+\Delta V_{nc}^{GB}}-1\right) \tag{6}$$

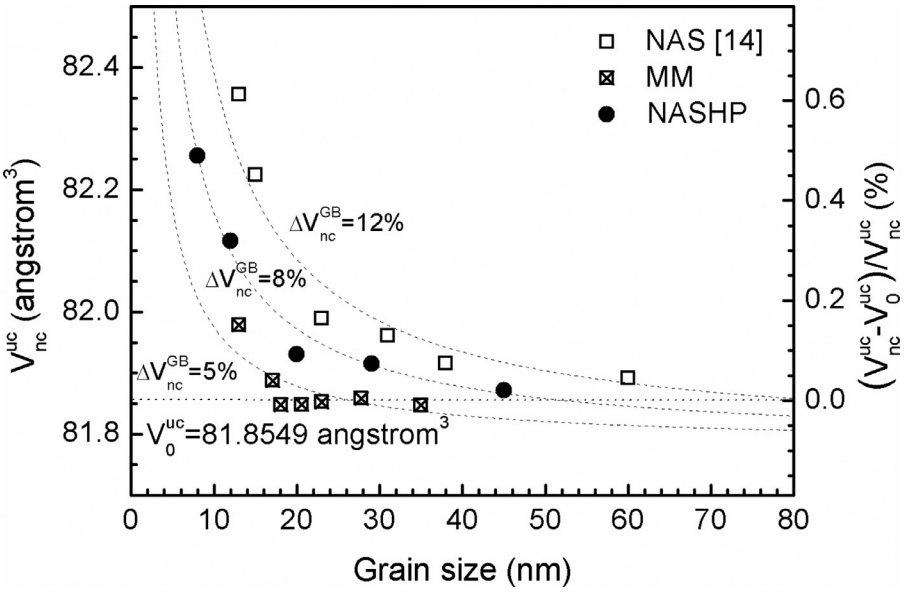

Fig. 10. Grain size dependence of the measured unit cell volume V_{nc}^{uc} and its deviations from the corresponding equilibrium values V_0^{uc} of the nc Se samples prepared by different synthesis methods. The dashed lines are the fitted curves according to Eq. (6) from which the excess GB volumes ΔV_{nc}^{GB} are 12%, 8% and 5% for NAS, NASHP and MM prepared nc Se.

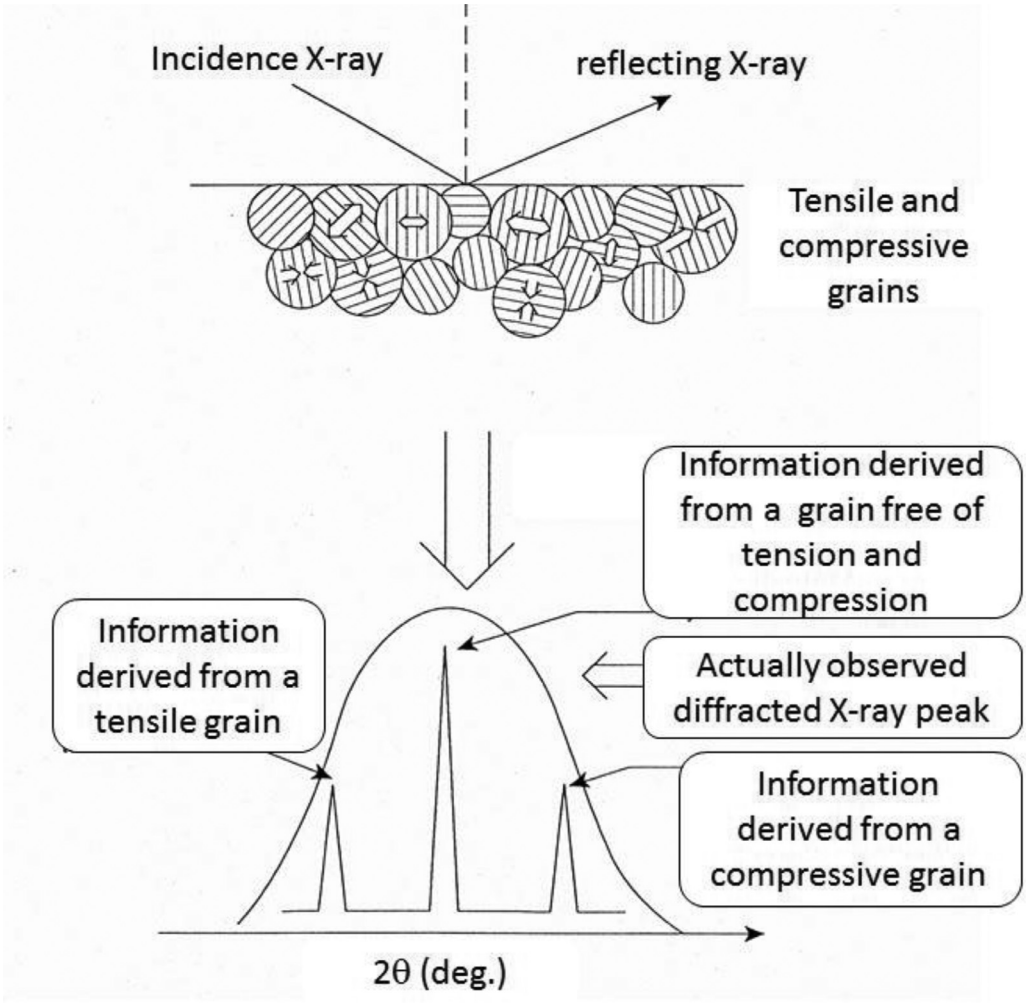

Fig. 11. Schematic representations of microstrain (calculated from XRD peak broadening) and lattice parameter (calculated from XRD peak position).

Table 4
A list of the GB excess volume ΔV_{nc}^{GB} in various nc samples processed by means of different techniques (IGC = inert gas condensation following by subsequent consolidation, MM = mechanical milling, NAS = nanocrystallization of amorphous solids, NASHP = NAS under high pressure).

Sample	D (nm)	Synthesis	Measurement	ΔV_{nc}^{GB} (%)	Reference
Pd	2.5	Modeling	Calculation	36	[28]
	8	IGC	Density measurement	20 (as-prepared) 14 (relaxed)	[59]
			Thermal expansion	10 (as-prepared) 5 (relaxed)	
Nb	10–5	Sputtering	XRD	27–33	[60]
	6	MM	XRD	16	[61]
Ni_3P	10–70	NAS	XRD	8–26	[62]
Se	13	MM	XRD	5	Present
	13	NAS		12	Present
	8	NASHP		8	Present

Table 5
A list of the GB expansion e_{GB} and calculated GB excess volume ΔV_{nc}^{GB} in various samples processed and measured by means of different techniques (MM = mechanical milling, SPD = severe plastic deformation, HREM = high resolution transmission electron microscopy, GG = grain growth, MD = molecular dynamic simulation).

Sample	D (nm)	Synthesis	Measurement	e_{GB} (10^{-10} m)	ΔV_{nc}^{GB} (%)	Reference
Au	Bicrystal	Crystal growth	HREM	0.04–0.1	0.12–0.3	[67]
				0.12	0.36	[68]
Al	Tricrystal	Crystal growth	GB tension	0.64	1.92	[69]
	Bicrystal	Crystal growth	HREM	0.2	0.6	[70]
Fe	60	MM	GG	0.19	0.1	[71]
Ge	Bicrystal	Crystal growth	HREM	0.1	0.3	[72]
NiO	Bicrystal	Crystal growth	HREM	0.4	1.2	[73]
Pd	15	Sputtering	XRD	1.7	3.4	[26]
Ni	26	Sputtering	XRD	1.6	1.8	[26]
	Σ5 GB	1200 K	MD	0.39–0.41	1.2–1.23	[74]
	Polycrystal	–		0.28–0.42	0.84–1.3	[75]
	175	SPD	GG	0.35	0.1	[76]

The GB width ξ is usually equal to 1 nm [50–52], and r_0 is equal to 2.373 Å for coarse-grained Se. The ΔV_{nc}^{GB} can be calculated by fitting the experimentally measured V_{nc}^{uc} values using Eq. (6), as plotted in dashed lines in Fig. 6. The ΔV_{nc}^{GB} of nc Se prepared by NAS, NASHP and MM methods are 12%, 8% and 5%, respectively. Moreover, ΔV_{nc}^{GB} of cubic crystals could be calculated from the lattice expansion based on Eq. (5), as listed in Table 1. In addition, the experimental values of ΔV_{nc}^{GB} reported in literature were also summarized in Table 4 [28,59–62]. It can be seen that ΔV_{nc}^{GB} exhibits similar elemental and preparation dependences with the lattice expansion listed in Table 1. Bottom-up preparations, such as IGC, NAS, sputtering, etc., experience large volume shrinking processes and therefore produce large ΔV_{nc}^{GB} in range of 10–30%, while top-down methods, such as MM, produce a much small ΔV_{nc}^{GB} less than 10% and most values are less than 3%. The ΔV_{nc}^{GB} values of metals calculated from the lattice expansion (most are less than 3%) is usually one order of magnitude smaller than those of metalloids and compounds (larger than 5%), such as Se, Si, Ge, etc. with large amount of dangling bonds at the GBs. Specifically, the different ΔV_{nc}^{GB} of the nc Se samples in the present study can be understood qualitatively from their synthesis methods. The NAS of Se is accompanied by a large volume shrinking process, which generates large amount of vacancies and/or vacancy clusters at GBs [22]. The NAS under high pressure can annihilate some vacancies and/or vacancy clusters during volume shrinking process, resulting in a smaller ΔV_{nc}^{GB} (8%). The grain refinement process of crystalline Se by the MM method introduces a volume expansion, and therefore corresponds to the smallest ΔV_{nc}^{GB} (5%).

The lattice contraction or negative ΔV_{nc}^{GB} listed in Table 1 might be caused by the presence of surface curvature pressure based on the Gibbs–Thomson effect [63]. In literature, lattice contraction was frequently observed in isolated nano-particles due to surface stress [64], which induces more hydrostatic compression on the nano-particle as compared to micron-size particles. The change in the unit cell volume ΔV^{uc} can be expressed as:

$$\frac{\Delta V^{uc}}{V_0^{uc}} = -\frac{4\sigma}{K D} \tag{7}$$

where V_0^{uc} is the coarse-grained unit cell volume, σ is the surface energy, K is the bulk modulus and D is the spherical particle diameter. It was reported that when ZrO_2 nano-particles with surface were consolidated into nanocrystalline solids with GBs via spark plasma sintering (SPS), lattice distance experienced a transformation from contraction to expansion [65,66]. This experiment suggests that the lattice contraction or negative ΔV_{nc}^{GB} observed in nc materials might be caused by large amount of macro-voids or pores at GBs, which damaged the atomic bonds at GBs and produced surface-like effect as nano-particles. Therefore, the measured lattice parameter was the result of two competing mechanisms: surface-stress-induced lattice contraction vs. expansion by the GB stress field due to the increased excess free volume [33].

5.3. GB expansion e_{GB}

An alternative quantity related with GB excess volume ΔV_{nc}^{GB} is GB expansion, e_{GB}, which was defined as the excess volume V per unit of GB area A,

$$e_{GB} = \left(\frac{\partial V}{\partial A}\right)_{T,p,n_i} \tag{8}$$

at constant temperature T and pressure p, and for a constant number n_i of atoms. Assuming that nc polycrystal consists of square-shaped nanocrystallites with orthogonal GB systems, ΔV_{nc}^{GB} and e_{GB} have the follow-

ing relationship,

$$\Delta V_{nc}^{GB} = \frac{3e_{GB}}{D} \quad (9)$$

The GB expansion can be measured by different techniques, such as high resolution transmission electron microscopy (HREM), grain growth (GG), XRD, etc., as summarized in Table 5. One can see that e_{GB} are ranging from 0.04×10^{-10} m (Au measured from HREM [67]) to 0.64×10^{-10} m (Al tricrystal measured from the pressure dependence of GB surface tension [69]). Exceptionally large values of e_{GB} for magnetron sputtered Ni (1.6×10^{-10} m) and Pd (1.7×10^{-10} m) thin films with 50 nm thick might be caused by the external residual stress. ΔV_{nc}^{GB}, calculated from e_{GB} assuming $D = =10$ nm, are ranging from 0.10% to 1.92%, agreeing well with the ΔV_{nc}^{GB} calculated from the lattice expansion, as listed in Table 1.

6. Conclusion

In summary, by quantitative XRD measurements we revealed that the lattice constants of nc Se increase with decreasing grain size. This phenomenon occurred in nc Se prepared by mechanical milling of crystalline Se and nanocrystallization of amorphous Se under high pressure, suggesting that the lattice expansion in nc Se is intrinsic. The magnitude of lattice expansion depends on the processing method, because the GB structure is affected by the way these GBs were created (i.e. the processing method). A GB stress field model was able to satisfactorily describe the grain-size dependence of the lattice constants, and the GB excess volume calculated by the model also shows processing method dependence.

Declaration of Competing Interest

The authors declare that they have no known competing financial interests or personal relationships that could have appeared to influence the work reported in this paper.

Acknowledgments

Y.H. Zhao acknowledges financial supports from the National Key R&D Program of China (Grant No. 2017YFA0204403) and National Natural Science Foundation of China (Grant No. 51971112 and 51225102) as well as the Fundamental Research Funds for the Central Universities (Grant No. 30919011405),

References

[1] I. Dirba, P. Komissinskiy, O. Gutfleisch, L. Alff, Increased magnetic moment induced by lattice expansion from α-Fe to α'-Fe_8N, J. Appl. Phys. 117 (2015) 173911.
[2] D. Passarello, J. Jeong, M.G. Samant, S.S.P. Parkin, Depth-dependent giant lattice expansion of up to 5% in ionic liquid-gated 90 nm thick VO_2 (001)/Al_2O_3 (10-10) films, Appl. Phys. Lett. 107 (2015) 201906.
[3] V.I. Razumovskiy, A. Reyes-Huamantinco, P. Puschnig, A.V. Ruban, Effect of thermal lattice expansion on the stacking fault energies of fcc Fe and $Fe_{75}Mn_{25}$ alloy, Phys. Rev. B 93 (2016) 054111.
[4] E. Gaffet, M. Harmelin, Crystal-amorphous phase transition induced by ball-milling in silicon, J. Less Common Met. 157 (1990) 201–222.
[5] T.D. Shen, C.C. Koch, T.L. Mccormick, R.J. Nemanich, J.Y. Huang, J.G. Huang, The structure and property characteristics of amorphous/nanocrystalline silicon produced by ball milling, J. Mater. Res. 10 (1995) 139–148.
[6] E. Gaffet, Phase transition induced by ball milling in germanium, Mater. Sci. Eng. A 136 (1991) 161–169.
[7] Y.H. Zhao, Z.H. Jin, K. Lu, Mechanical-milling-induced amorphization of Se: a crystallite destabilization model, Phil. Mag. Lett. 79 (1999) 747–754.
[8] Y.H. Zhao, K. Lu, T. Liu, EXAFS study of mechanical-milling-induced solid-state amorphization of Se, J. Non Cryst. Solids 333 (2004) 246–251.
[9] Y.H. Zhao, Y.T. Zhu, T. Liu, Mechanism of solid-state amorphization of Se induced by mechanical milling, J. Appl. Phys. 95 (2004) 7674–7680.
[10] J. Buckeridge, D.O. Scanlon, A. Walsh, C.R.A. Catlow, A.A. Sokol, Dynamical response and instability in ceria under lattice expansion, Phys. Rev. B 87 (2013) 3249–3253.
[11] Y.F. Zhu, W.T. Zheng, Q. Jiang, Modeling lattice expansion and cohesive energy of nanostructured materials, Appl. Phys. Lett. 95 (2009) 083110.
[12] Y.F. Zhu, W.T. Zheng, Q. Jiang, Distinct young's modulus of nanostructured materials in comparison with nanocrystals, Phys. Chem. Chem. Phys. 13 (2011) 21328–21332.
[13] Z.M. Wang, J.Y. Wang, L.P.H. Jeurgens, F. Phillipp, E.J. Mittemeijer, Origins of stress development during metal-induced crystallization and layer exchange: annealing amorphous ge/crystalline al bilayers, Acta Mater. 56 (2008) 5047–5057.
[14] Y.H. Zhao, K. Zhang, K. Lu, Structure characteristics of nanocrystalline element selenium with different grain sizes, Phys. Rev. B 56 (1997) 14322–14329.
[15] F. Hofmann, D. Nguyen-Manh, M.R. Gilbert, C.E. Beck, J.K. Eliason, A.A. Maznev, W. Liu, D.E.J. Armstrong, K.A. Nelsond, S.L. Dudarev, Lattice swelling and modulus change in a helium-implanted tungsten alloy: x-ray micro-diffraction, surface acoustic wave measurements, and multiscale modelling, Acta Mater. 89 (2015) 352–363.
[16] J. Sheng, U. Welzel, E.J. Mittemeijer, Nonmonotonic crystallite-size dependence of the lattice parameter of nanocrystalline nickel, Appl. Phys. Lett. 97 (2010) 153109.
[17] S. Tiemeyer, M. Bombeck, H. Göhring, M. Paulus, C. Sternemann, J. Nase, F.J. Wirkert, J. Möller, T. Büning, O.H. Seeck, D. Reuter, A.D. Wieck, M. Bayer, M. Tolan, Polaron-induced lattice distortion of (In, Ga)As/GaAs quantum dots by optically excited carriers, Nanotechn. 27 (2016) 425702.
[18] F. Börrnert, A. Barreiro, D. Wolf, M.I. Katsnelson, B. Büchner, L.M.K. Vandersypen, M.H. Rümmeli, Lattice expansion in seamless bilayer graphene constrictions at high bias, Nano Lett. 12 (2012) 4455–4459.
[19] H. Gleiter, Nanocrystalline materials, Prog. Mater. Sci. 33 (1989) 223–315.
[20] M.A. Meyers, A. Mishra, D.J. Benson, Mechanical properties of nanocrystalline materials, Prog. Mater. Sci. 51 (2006) 427–556.
[21] T. Haubold, R. Birringer, B. Lengeler, H. Gleiter, Exafs studies of nanocrystalline materials exhibiting a new solid state structure with randomly arranged atoms, Phys. Lett. A 135 (1989) 461–466.
[22] M.L. Sui, K. Lu, W. Deng, L.Y. Xiong, S. Patu, Y.Z. He, Positron-lifetime study of polycrystalline Ni-P alloys with ultrafine grains, Phys. Rev. B 44 (1991) 6466–6471.
[23] H.E. Schaefer, R. Wurschum, R. Birringer, H. Gleiter, Structure of nanometer-sized polycrystalline iron investigated by positron lifetime spectroscopy, Phys. Rev. B 38 (1988) 9545–9554.
[24] S. Van Petegem, F. Dalla Torre, D. Segers, H. Van Swygenhoven, Free volume in nanostructured Ni, Scr. Mater. 48 (2003) 17–22.
[25] W. Wunderlich, Y. Ishida, R. Maurer, HREM-studies of the microstructure of nanocrystalline palladium, Scr. Metall. Mater. 24 (1990) 403–408.
[26] Y. Kuru, M. Wohlschlogel, U. Welzel, E.J. Mittemeijer, Large excess volume in grain boundaries of stressed, nanocrystalline metallic thin films: its effect on grain-growth kinetics, Appl. Phys. Lett. 95 (2009) 163112.
[27] M. Wagner, Structure and thermodynamic properties of nanocrystalline metals, Phys. Rev. B 45 (1992) 635–639.
[28] H.J. Fecht, Intrinsic instability and entropy stabilization of grain boundaries, Phys. Rev. Lett. 65 (1990) 610–613.
[29] B. Baretzky, M.D. Baro, G.P. Grabovetskaya, J. Gubicza, M.B. Ivanov, Y.R. Kolobov, et al., Fundamentals of interface phenomena in advanced bulk nanoscale materials, Rev. Adv. Mater. Sci. 9 (2005) 45–108.
[30] A.A. Nazarov, A.E. Romanov, R.Z. Valiev, On the structure, stress fields and energy of nonequilibrium grain boundaries, Acta Metall. Mater. 41 (1993) 1033–1040.
[31] H.Y. Zhang, K. Lu, Z.Q. Hu, Formation and lattice distortion of nanocrystalline selenium, Nanostruct. Mater. 6 (1995) 489–492.
[32] J.A. Eastman, M.R. Fitzsimmons, On the two-state microstructure of nanocrystalline chromium, J. Appl. Phys. 77 (1995) 522–527.
[33] G.K. Rane, U. Welzel, S.R. Meka, E.J. Mittemeijer, Non-monotonic lattice parameter variation with crystallite size in nanocrystalline solids, Acta Mater. 61 (2013) 4524–4533.
[34] K. Zhang, I.V. Alexandrov, R.Z. Valiev, K. Lu, Structural characterization of nanocrystalline copper by means of x-ray diffraction, J. Appl. Phys. 80 (1996) 5617–5624.
[35] Y.H. Zhao, K. Lu, K. Zhang, Microstructure evolution and thermal properties in nanocrystalline Cu during mechanical attrition, Phys. Rev. B 66 (2002) 085404.
[36] R. Birringer, M. Hoffmann, P. Zimmer, Interface stress in polycrystalline materials: the case of nanocrystalline Pd, Phys. Rev. Lett. 88 (2002) 206104.
[37] R. Divakar, V.S. Raghunathan, Characterisation of interfaces in nanocrystalline palladium, Acad. P. Eng. S. 28 (2003) 47–62.
[38] J.I. Langford, R. Delhez, Th.H. de Keijser, E.J. Mittemeijer, Profile analysis for microcrystalline properties by the Fourier and other methods, Australian J. Phys. 41 (1988) 173–187.
[39] H.M. Isomaki, J. von Boehm, Pressure dependence of the permittivity of trigonal Se and Te, Phys. Rev. B 35 (1987) 8019–8023.
[40] D.E. Cox, J.B. Hastings, L.P. Cardoso, L.W. Finger, Synchrotron x-ray powder diffraction at X13A: a dedicated powder diffractometer at the national synchrotron light source, Mater. Sci. Forum. 9 (1986) 1–20.
[41] H.P. Klug, L.E. Alexander, in: X-ray Diffraction Procedures For Polycrystalline and Amorphous Materials, 2nd ed., John Wiley and Sons, New York, 1974, p. 491.
[42] P.R. Bevington, Data Reduction and Error Analysis For the Physical Sciences, McGraw-Hill, New York, 1969.
[43] J. Labell, A. Zagofsky, S. Pearlman, Cu Kα2 elimination algorithm, J. Appl. Cryst. 8 (1975) 499–506.
[44] G. Platbrood, Kα2 elimination algorithm for Cu, Co and Cr radiations, J. Appl. Cryst. 16 (1983) 24–27.
[45] F. Ye, K. Lu, Pressure effect on polymorphous crystallization kinetics in amorphous selenium, Acta Mater. 46 (1998) 5965–5971.
[46] M.Y. Gamarnik, Change of lattice parameters in highly disperse nickel powders, Phys. Status Solidi B 168 (1991) 389–395.
[47] J.S. Vermaak, C.W. Mays, D. Kuhlmann-Wilsdorf, On surface stress and surface tension: I. theoretical considerations, Surf. Sci. 12 (1968) 128–133.

[48] J. Weissmuller, J.W. Cahn, Mean stresses in microstructures due to interface stresses: a generalization of a capillary equation for solids, Acta Mater. 45 (1997) 1899–1906.
[49] M.L. Sui, L.Y. Xiong, W. Deng, Investigation of the interfacial defects in a nanocrystalline Ni-P alloy by positron annihilation spectroscopy, J. Appl. Phys. 69 (1991) 4451–4453.
[50] W. Qin, Z.H. Chen, P.Y. Huang, Y.H. Zhuang, Crystal lattice expansion of nanocrystalline materials, J. Alloys Comp. 292 (1999) 230–232.
[51] W. Qin, T. Nagase, Y. Umakoshi, J.A. Szpunar, Lattice distortion and its effects on physical properties of nanostructured materials, J. Phys. Cond. Matter. 19 (2007) 236217.
[52] W. Qin, T. Nagase, Y. Umakosh, J.A. Szpunar, Relationship between microstrain and lattice parameter change in nanocrystalline materials, Phil. Mag. Lett. 88 (2008) 169–179.
[53] K. Lu, M.L. Sui, Is the crystalline lattice structure in nanocrystalline materials different from the perfect crystal lattice? J. Mater. Sci. Techn. 9 (1993) 419–422.
[54] H.J. Fecht, Thermodynamic properties and stability of grain boundaries in metals based on the universal equation of state at negative pressure, Acta Metall. Mater. 38 (1990) 1927–1932.
[55] H.E. Schaefer, R. Wurschum, R. Birringer, H. Gleiter, Nanometre-sized solids, their structure and properties, J. Less Common Met. 140 (1988) 161–169.
[56] M.J. Zehetbauer, G. Steiner, E. Schafler, A. Korznikov, E. Korznikova, Deformation induced vacancies with severe plastic deformation: measurements and modelling, Mater. Sci. Forum 503 (2006) 57–64.
[57] H. Kronmuller, M. Fahnle, M. Domann, H. Grimm, R. Grimm, B. Groger, Magnetic properties of amorphous ferromagnetic alloys, J. Magn. Magn. Mater. 13 (1979) 53–70.
[58] , The Physics of Metals, in: D. Feng (Ed.), The Physics of Metals, Scientific Press, Beijing, 1987, p. 173.
[59] R. Birringer, E. Krill, M. Klingel, Orientation-phase-space-averaged properties of grain boundaries, Phil. Mag. Lett. 72 (1995) 71–77.
[60] D. Hazra, S. Datta, M. Mondal, J. Ghatak, P.V. Satyam, A.K. Gupta, Thickness dependent lattice expansion in nanogranular Nb thin films, J. Appl. Phys. 103 (2008) 103535.
[61] P.P. Chattopadhyay, P.M.G. Nambissan, S.K. Pabi, I. Manna, Polymorphic bcc to fcc transformation of nanocrystalline niobium studied by positron annihilation, Phys. Rev. B 63 (2001) 054107.
[62] K. Lu, Interfacial structural characteristics and grain-size limits in nanocrystalline materials crystallized from amorphous solids, Phys. Rev. B 51 (1995) 18–27.
[63] J.W. Gibbs, Collected Works, Longmans, Green & Co., New York, 1928.
[64] C.Q. Sun, Thermo-mechanical behavior of low-dimensional systems: the local bond average approach, Prog. Mater. Sci. 54 (2009) 179–307.
[65] E.K. Akdogan, I. Savklıyıldız, H. Bicer, W. Paxton, F. Toksoy, Z. Zhong, T. Tsakalakos, Anomalous lattice expansion in yttria stabilized zirconia under simultaneous applied electric and thermal fields: a time-resolved in situ energy dispersive x-ray diffractometry study with an ultrahigh energy synchrotron probe, J. Appl. Phys. 113 (2013) 233503.
[66] M.B. Ponnuchamy, A.S. Gandhi, Lattice expansion and contraction in nanocrystalline yttria-stabilized zirconia powders, Scr. Mater. 83 (2014) 21–24.
[67] K.L. Merkle, Quantification of atomic-scale grain boundary parameters by high resolution electron microscopy, Ultramicroscopy 40 (1992) 281–290.
[68] M.I. Buckett, K.L. Merkle, Determination of grain boundary volume expansion by HREM, Ultramicroscopy 56 (1994) 71–78.
[69] L.S. Shvindlerman, G. Gottstein, V.A. Ivanov, D.A. Molodov, D. Kolesnikov, W. Lojkowski, Grain boundary excess free volume – direct thermodynamic measurement, J. Mater. Sci. 41 (2006) 7725–7729.
[70] R.C. Pond, Periodic grain boundary structures in aluminium. II. a geometrical method for analysing periodic grain boundary structure and some related transmission electron microscope observations, Proc. R. Soc. London, Ser. B 357 (1977) 471–483.
[71] C.E. Krill, L. Helfen, D. Michels, H. Natter, A. Fitch, O. Masson, R. Birringer, Size-dependent grain-growth kinetics observed in nanocrystalline Fe, Phys. Rev. Lett. 86 (2001) 842–845.
[72] H.J. Leamy, G.E. Pike, C.H. Seager, Grain Boundaries in Semiconductors, Elsevier, New York, 1982 North-Holland, Amsterdam.
[73] K.L. Merkle, D.J. Smith, Atomic structure of symmetric tilt grain boundaries in NiO, Phys. Rev. Lett. 59 (1987) 2887–2890.
[74] H. Zhang, D.J. Srolovitz, Simulation and analysis of the migration mechanism of Σ5 tilt grain boundaries in an fcc metal, Acta Mater. 54 (2006) 623–633.
[75] D.L. Olmsted, S.M. Foiles, E.A. Holm, Survey of computed grain boundary properties in face-centered cubic metals: I. grain boundary energy, Acta Mater. 57 (2009) 3694–3703.
[76] E.M. Steyskal, B. Oberdorfer, W. Sprengel, M. Zehetbauer, R. Pippan, R. Wurschum, Direct experimental determination of grain boundary excess volume in metals, Phys. Rev. Lett. 108 (2012) 055504.